Global-scale simulation of foreshock structures at the quasi-parallel bow shock

Y. Lin

Physics Department, Auburn University, Auburn, Alabama, USA

Received 15 April 2003; revised 24 July 2003; accepted 8 August 2003; published 1 November 2003.

[1] A two-dimensional, global-scale hybrid simulation is carried out to study the kinetic structure of the quasi-parallel bow shock. In the simulation the bow shock forms by the interaction of the supersonic solar wind and the geomagnetic field. Strong temporal electromagnetic waves occur in the shock transition and foreshock regions due to backstreaming and reflected ions at the bow shock. This self-consistent, global-scale simulation shows the formation of diamagnetic cavities in the foreshock regions of the parallel and quasi-parallel shocks, where ion beams interact with the incoming solar wind plasma. The cavities are crater-like and saturate at a width $\sim 1-2\ R_E$, with a low-density and low-magnetic field center bounded by a rim of high density and high magnetic field. The bulk flow speed decreases slightly in the center of the cavity, while the ion temperature often, but not always, increases. The craters convect downstream with the solar wind flow. When the interplanetary magnetic field (IMF) lies nearly parallel to the solar wind flow, the craters develop into elongated phase-standing spatial structures along the field lines, both upstream and downstream, with alternate increases and decreases in the density and corresponding in-phase variations in the magnetic field strength. In the general cases with an oblique IMF the foreshock cavities can convect toward the Earth as transient compressional structures and impinge on the magnetopause. The generation and structure of the diamagnetic cavities are compared with those of hot flow anomalies. The simulation results are also compared with satellite observations of the foreshock of quasi-parallel shocks. *INDEX TERMS:* 2154 Interplanetary Physics: Planetary bow shocks; 2159 Interplanetary Physics: Plasma waves and turbulence; 2753 Magnetospheric Physics: Numerical modeling; 2784 Magnetospheric Physics: Solar wind/magnetosphere interactions; 7867 Space Plasma Physics: Wave/particle interactions; *KEYWORDS:* bow shock, magnetosheath, kinetic structure, numerical simulation, nonlinear wave-particle interaction, pressure pulses

Citation: Lin, Y., Global-scale simulation of foreshock structures at the quasi-parallel bow shock, *J. Geophys. Res.*, *108*(A11), 1390, doi:10.1029/2003JA009991, 2003.

1. Introduction

[2] The structure of the Earth's bow shock [*Cahill and Patel*, 1967] has been of great interest for decades because the bow shock is the frontier in the interaction between the solar wind and the magnetosphere. The bow shock has been divided into two classes according to its shock normal angle θ_{Bn}, which is the angle between the shock normal direction **n** and the upstream interplanetary magnetic field (IMF) $\mathbf{B}_0$. They are the quasi-parallel shock with $\theta_{Bn} < 45^\circ$ and the quasi-perpendicular shock with $\theta_{Bn} > 45^\circ$. Satellite observations and kinetic simulations have shown that the structure and ion heating of the bow shock are in general very different in quasi-parallel and quasi-perpendicular shocks [*Leroy and Winske*, 1983; *Gosling and Robson*, 1985; *Goodrich*, 1985; *Scholer and Terasawa*, 1990].

[3] In the quasi-parallel shocks the solar wind ions can be reflected into upstream nearly along field lines, and backstreaming ions from the downstream can escape a large distance in the foreshock region. Near the shock transition the instabilities due to interactions between ion beams contribute to the energy dissipation required by the shock [*Tanaka et al.*, 1983; *Sckopke et al.*, 1983]. It is believed that first-order Fermi acceleration of ions between upstream waves and the shock leads to ion heating and energetic ions at quasi-parallel shocks [e.g., *Lee*, 1982; *Fuselier et al.*, 1995], yielding the so-called bow shock diffuse ions. Pressure pulses and the associated magnetic field variations can be generated in the foreshock regions by processes within the bow shock [*Fairfield et al.*, 1990; *Sibeck et al.*, 2001], with positively correlated variations in magnetic field and plasma density. The thermal pressure of energized foreshock ions can reach 40% of that in the ambient solar wind [*Asbridge et al.*, 1968]. Given that the foreshock activities can lead to transient pressure pulses at the Earth's magnetopause, corresponding to compressions or rarefactions in the dayside magnetospheric magnetic field [e.g., *Fairfield et al.*, 1990; *Sibeck et al.*, 2003] and be linked to ULF pulsations [*Russell et al.*, 1983; *Engebretson et al.*,

0148-0227/03/2003JA009991

1991] in the magnetosphere, understanding the spatial structures and temporal variations of quasi-parallel shocks is particularly important to magnetospheric physics. The physics related to quasi-parallel shocks is our main concern in this paper.

[4] Hybrid simulations have been carried out for the nonlinear structure and ion heating of quasi-parallel shocks [e.g., *Goodrich*, 1985; *Onsager et al.*, 1991; *Thomas et al.*, 1990; *Winske et al.*, 1990; *Scholer and Terasawa*, 1990; *Lyu and Kan*, 1990; *Scholer*, 1993; *Scholer et al.*, 1993; *Krauss-Varban*, 1995]. The hybrid codes include full ion kinetics and have been used to study various collisionless shocks. These simulations have revealed important features of collisionless fast shocks, such as the presence of reflected/backstreaming ions at the shock and their roles in the shock structure and ion heating. In addition to the whistler waves associated with the fast mode shock, the interaction between backstreaming ion beams and the ambient plasmas is also found to lead to the generation of large-amplitude electromagnetic waves in the upstream and downstream regions. The structure of quasi-parallel shocks, in general, is found to evolve dynamically due to the wave-particle interaction [e.g., *Dubouloz and Scholer*, 1995], consistent with observations at the bow shock [*Hoppe et al.*, 1981; *Schwartz et al.*, 1992].

[5] Most of the previous simulations, however, are based on planar bow shock fronts and many are one-dimensional (1-D). In the 1-D models the spatial variations can only be in the shock normal direction, and thus the normal component, B_n, of magnetic field is constant everywhere according to the Maxwell equations. The 1-D models may be particularly inappropriate for parallel shocks, in which the tangential component of the magnetic field is nearly zero. Since the foreshock regions are found to be more active in quasi-parallel or parallel shocks, and the dynamic processes at these shocks exist over some distance into the upstream solar wind, a large-scale and multi-dimensional model is necessary to simulate parallel and quasi-parallel shocks. A two-dimensional global-scale hybrid simulation of the bow shock-magnetosheath-magnetosphere system is carried out in this study for the structure of the curved bow shock in front of the magnetosphere.

[6] Previously, we studied the interaction between interplanetary discontinuities and the bow shock using a similar 2-D hybrid simulation in a curvilinear coordinate system [*Lin et al.*, 1996; *Lin*, 1997, 2002]. These simulations aimed at the generation of transient plasma structures near and in the magnetosphere due to external magnetic perturbations in the solar wind. In particular, our simulations showed that hot flow anomalies (HFAs), or hot diamagnetic cavities, can be generated near the bow shock by the kinetic interaction between the shock and an incident tangential discontinuity that carries a change in the IMF direction. The simulation results were consistent with the observed structure of HFA [e.g., *Schwartz et al.*, 1988]. The present paper, on the other hand, aims at another important aspect of the transient processes through the bow shock: the foreshock and bow shock transients generated internally in the shock itself. In the previous simulation by *Lin* [2002], it was found that beside HFAs, some spatial structures with alternate temperature increases (density decreases) and decreases (temperature increases) developed at the quasi-parallel shock. Those with temperature increases and flow speed decreases appeared like weak HFAs. Nevertheless, unlike the HFA, these structures were not generated by the arrival of the external discontinuity.

[7] On the other hand, observations indicated that diamagnetic cavities, or crater-like structures, are frequently present in foreshock regions of quasi-parallel shocks [*Wibberenz et al.*, 1985; *Sibeck et al.*, 1989; *Fairfield et al.*, 1990; *Sibeck et al.*, 2001, 2002]. *Sibeck et al.* [2001] presented a statistical survey of foreshock events using plasma, magnetic field, and energetic ion observations by IMP 8. Pressures associated with the energetic ions were found to depress the foreshock magnetic field strength and plasma densities. The cavities occurred preferentially during high-speed solar wind streams, but unlike HFAs, they showed no clear dependence upon other solar wind parameters. Moreover, these events were more common than HFA: many events occurred per day. In a further study based on Wind observations, *Sibeck et al.* [2002] compared the observed foreshock cavities with a hybrid simulation by *Thomas and Brecht* [1988] for the interaction of a spatially limited beam of backstreaming ions with the incoming solar wind and attributed the cavities to the diamagnetic effects of ions Fermi accelerated within the foreshock. The hybrid simulation by *Thomas and Brecht* [1988] showed that the beam-plasma interaction can create crater-like, in-phase magnetic field and ion density structures, with depressed (enhanced) plasma density and magnetic field at the center (on the edges) of the cavity.

[8] In this paper, we focus our investigation on the generation of foreshock structures and their evolution due to internal processes in the bow shock. The main purpose is to report for the first time that diamagnetic cavities can be generated self-consistently in the foreshock regions of the part of curved shock front where the shock is of quasi-parallel geometry. The cavity-like structures then evolve and extend into the downstream regions. The outline of the paper is as the following. The simulation model is described in section 2. The simulation results are presented in section 3. A summary is given in section 4.

2. Simulation Model

[9] The hybrid code used in this study was developed by *Swift* [1996] and used in our previous global simulations [e.g., *Lin et al.*, 1996; *Lin*, 2002]. In the hybrid code, the ions (protons) are treated as discrete particles, and the electrons are treated as a massless fluid. Quasi charge neutrality is assumed in the simulation. The simulation includes the entire system of the bow shock, magnetosheath, and magnetosphere on the dayside. The 2-D ($\partial/\partial_y = 0$) simulation is carried out in the noon-midnight meridian plane, in which the x axis points along the Sun-Earth line and toward the Sun, and the z axis points from south to north. A polar coordinate system is used in the simulation; this system consists of the radial distance r in the xz plane and the polar angle $\theta \equiv \tan^{-1}(x/z)$. The Earth is located at the origin $(x, z) = (0, 0)$. The simulation domain lies within the region with $5\ R_E < r < 30\ R_E$ and $0^\circ \leq \theta \leq 180^\circ$.

[10] In most regions of the simulation domain, except the inner magnetosphere with $r < 6\ R_E$ where a cold, dense ion fluid is applied, the equation for ion motion is given as

$$d\frac{\mathbf{v}_i}{dt} = \mathbf{E} + \mathbf{v}_i \times \mathbf{B} - \nu(\mathbf{V}_i - \mathbf{V}_e) \quad (1)$$

where $\mathbf{v}_i$ is the ion particle velocity, $\mathbf{E}$ is the electric field in units of ion acceleration, $\mathbf{B}$ is the magnetic field in units of the ion gyrofrequency, ν is the collision frequency which can be applied to the magnetopause for possible magnetic reconnection, and $\mathbf{V}_e$ and $\mathbf{V}_i$ are the bulk flow velocities of electrons and ions, respectively. The electric field can be obtained from the electron momentum equation. The electron flow speed is evaluated from Ampere's law,

$$\mathbf{V}_e = \mathbf{V}_i - \frac{\nabla \times \mathbf{B}}{\alpha N} \quad (2)$$

where the charge coupling constant $\alpha = (4\pi e^2/m_i c^2)$, e is the electron charge, m_i is the ion mass, and N is the ion number density. The magnetic field is advanced in time from Faraday's law

$$\frac{\partial \mathbf{B}}{\partial t} = -\nabla \times \mathbf{E}. \quad (3)$$

[11] The ion gyrofrequency Ω_0 in the solar wind is chosen to be 0.6 s^{-1}, where $\Omega_0 = eB_0/m_i$, and B_0 is the magnitude of the IMF. This value of Ω_0 corresponds to an IMF $B_0 \sim 6$ nT. The number of ions per R_E^2 in the solar wind is chosen to be $N_0 = 4000 - 16{,}000$. In the calculation, the charge coupling constant α is a scaling parameter. The solar wind ion inertial length $\lambda_0 = c/\omega_{pi0} = 1/\sqrt{N_0\alpha}$, where ω_{pi0} is the ion plasma frequency, is chosen to be $0.04-0.08\ R_E$. Note that the Alfvén speed in the solar wind is $V_{A0} = \lambda_0\Omega_0$.

[12] In the simulation, a total of $\sim 2 \times 10^8$ particles are used in a run. The grids are uniformly distributed in the θ directions, with a total of 327–519 grid points. Nonuniform grid sizes Δr are used in the r direction, with a higher spatial resolution from the magnetosheath to the solar wind. The grid size $\Delta r \simeq 0.5\lambda_0$ for $r > 13\ R_E$. The time step for particle advance is $\Delta t = 0.002 - 0.02\Omega_0^{-1}$.

[13] Initially, the IMF and the ion particle density are assumed to be uniform for $r > 10\ R_E$. A 2-D dipole field plus an image dipole occupies the geomagnetic region within $r < 10\ R_E$. The dipole moment corresponds to a magnetic field of 40 nT at the magnetopause. The initial ion temperature is assumed to be isotropic, with $T_{m0} = 100T_0$, where T_{m0} and T_0 are the initial temperatures in the magnetosphere and the solar wind, respectively. The electron temperature is assumed to be zero for simplicity. In addition, a cold, dense fluid population occupies the magnetospheric region of $r < 6\ R_E$ to represent the dense plasma in the inner magnetosphere [*Swift*, 1996]. A perfect conducting boundary is assumed at the inner boundary at $r = 5\ R_E$.

[14] In the simulation, the solar wind flows along the $-x$ direction from the front side semicircular boundary at $r = 30\ R_E$ and convects the IMF $\mathbf{B}_0$ into the simulation domain. Outflow boundary conditions are used at the two straight line polar axes at $\theta = 0°$ (north) and $\theta = 180°$ (south) [*Swift*, 1996]. The bow shock, the magnetosheath, and the magnetopause boundary form from the interaction between the super-sonic solar wind and the magnetopause. Note that in general magnetic reconnection can occur in the magnetopause current sheet where antiparallel magnetic field components appear. In our simulation, a small current-dependent collision frequency is imposed along the magnetopause to play the role of resistivity [*Lin*, 2002]. The simulation results for the bow shock are found to be insensitive to the resistivity.

[15] Physical quantities are normalized as follows. The magnetic field B is normalized to the IMF B_0, the ion number density N is normalized to the solar wind density N_0, the flow velocity V is normalized to V_{A0}, and the time t is normalized to Ω_0^{-1}. The spatial coordinates are expressed in units of R_E. The thermal pressure is expressed in units of the magnetic pressure $P_{00} \equiv B_0^2/\alpha$, and the temperature is in units of $T_{00} \equiv P_{00}/N_0$.

3. Simulation Results of Cavity Structures and Filaments in the Foreshock and the Magnetosheath

[16] The simulation has been carried out for cases with an IMF cone angle of 0°, 10°, 15°, 30°, and 45°, and Alfvén Mach number $M_A = 5 - 8$. In the following, we present the simulation results for two cases. In case 1, the IMF cone angle is equal to 0°, whereas case 2 corresponds to a 30° IMF cone angle.

[17] In case 1, the IMF $B_{x0} = B_0$ and $B_{y0} = B_{z0} = 0$. This choice of the IMF pointing along the Sun-Earth line can result in the presence of quasi-parallel and parallel shocks in a large portion of the dayside domain so that the foreshock structure can be shown clearly. The solar wind ion plasma beta is chosen as $\beta_0 = 0.5$. The solar wind flow speed is assumed to be $V_0 = 5V_{A0}$, corresponding to a Mach number $M_A = 5$. The results shown correspond to $\lambda_0 = 0.08\ R_E$. The same run has also been performed for $\lambda_0 = 0.04\ R_E \simeq 250$ km, closer to the ion inertial length in reality, to make sure that similar results are obtained.

[18] Figure 1 shows the simulation results at $t = 48\Omega_0^{-1}$. Shown from the top are magnetic field lines plotted against the field magnitude on the logarithmic scale, contours of the B_y component of magnetic field, contour plot of the ion number density N, flow vectors plotted on top of the flow speed, and contours of the ion parallel temperature. Only part of the domain ($r \leq 26\ R_E$) is shown. At this time the bow shock is present at a standoff distance of $\sim 15\ R_E$ in front of the dayside magnetosphere, as seen from the enhanced ion density and magnetic field and the diverted flow vectors across the shock front. The entire low- and mid-latitude areas ($z < \pm 15\ R_E$) of the shock front in the simulation domain are dominated by quasi-parallel and near-parallel shocks. Downstream of the shock, the field lines in the magnetosheath drape around the magnetosphere, which occupies the dipole field region with $r < 10\ R_E$. Note that high-latitude magnetic reconnection between the magnetosheath and magnetospheric fields is seen in the Northern and Southern Hemispheres. This reconnection has no effects on the formation of the foreshock structures discussed below.

[19] Some crater-like structures are shown in the foreshock region upstream of the parallel and quasi-parallel

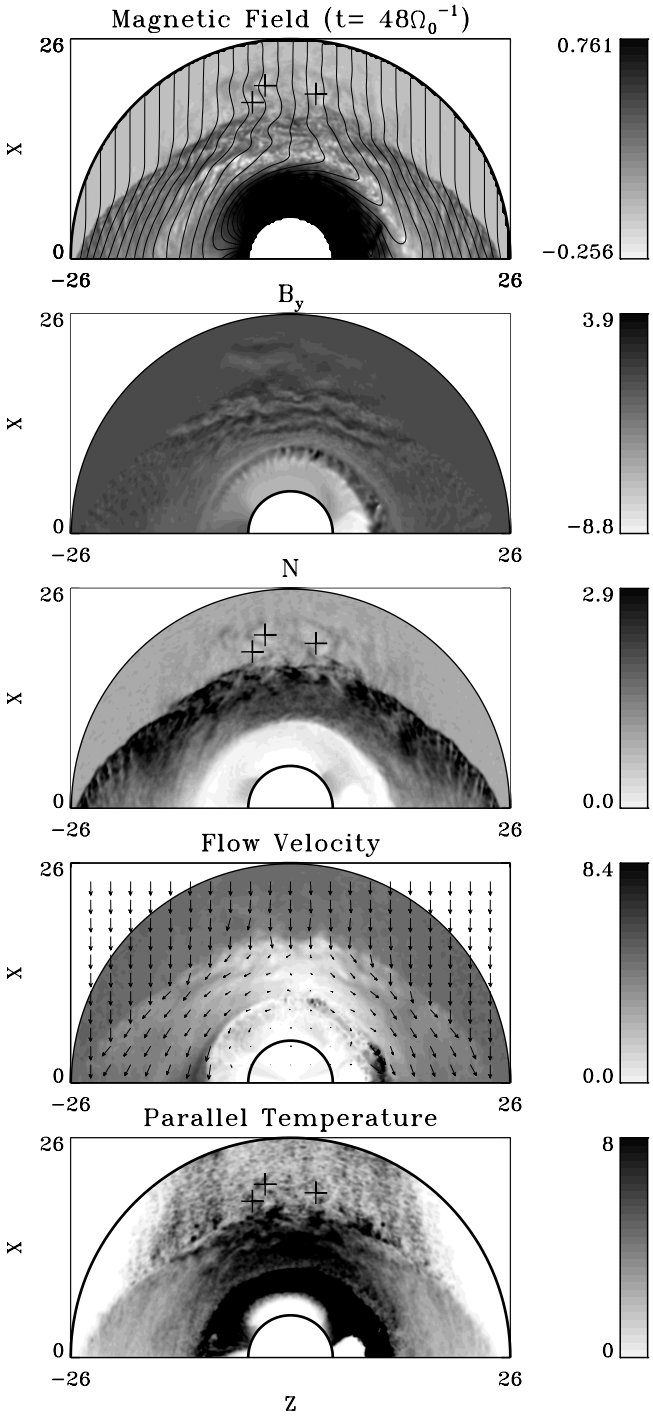

Figure 1. (From top) Magnetic field lines on top of the contours of field magnitude B on the logarithmic scale, contours of the B_y component of magnetic field, contours of ion number density N, flow vectors on top of the contours of flow speed, and contours of the ion parallel temperature at $t = 48\Omega_0^{-1}$ in case 1 with the IMF parallel to the solar wind flow. The cross marks indicate some of the diamagnetic cavities in the foreshock.

shocks, as shown in Figure 1. In these structures, a low density and low magnetic field diamagnetic cavity is surrounded by high density and high magnetic field strength. Some of the foreshock cavities are indicated in Figure 1 by the cross marks. The spatial variations in B and N are in phase and well correlated through these craters. For the three craters shown in Figure 1, at the rim of the craters B and N increase by a factor of 1.4 on average relative to those in the ambient solar wind. In the center of these craters they are ~75% of the average values in the solar wind. The flow speed also decreases (by ~13%) in the diamagnetic cavities but not as obvious as B and N. The width of the diamagnetic cavities is ~1–2 R_E.

[20] These crater-like structures exist in the region where backstreaming ions, often associated with a diffuse ion distribution in the foreshock, are present. At the quasi-parallel shock, the solar wind ions can be reflected by the shock, with guiding center motion following field lines upstream, and the downstream thermal ions can also backstream into the upstream region. Similar to previous studies, large-amplitude electromagnetic waves are generated in the vicinity of the shock due to this interaction between the background plasma and the counterstreaming ion beams. In addition, particle scattering between the upstream and downstream waves provides a mechanism for Fermi acceleration of the reflected/backstreaming solar wind ions, leading to the (not fully developed) diffuse foreshock ion distribution in phase space. Overall, the sunward, hot ion beam can escape a large distance (>10 R_E from the shock) following field lines in the upstream. As seen in Figure 1, parallel temperatures upstream from the quasi-parallel shock are much larger than those at the quasi-perpendicular shock. Consistent with previous hybrid simulations of the bow shock, the quasi-parallel shocks are found to constantly go through a reformation, i.e., steepening, cycle [*Burgess*, 1989] due to the transient waves near the shock front. This process occurs within a width of ~1 R_E upstream from the shock front, and the period of the cycle is ~20–40Ω_0^{-1} over the range of latitudes. Note that large-amplitude transient pulsations with much shorter periods [e.g., *Dubouloz and Scholer*, 1995] are also found in the foreshock in early times after the shock forms and near the shock ramp in later times.

[21] The presence of the craters in the foreshock is associated with the interaction between the hot, tenuous, sunward ion beam and the dense, incoming solar wind plasma, with relative speeds between the two population $\gg$ local Alfvén speed. In the foreshock region where the craters are seen, the density of the hot beam ions is ~6–20% of that of the background solar wind. In early times with $t < 60\Omega_0^{-1}$, fast compressional magnetosonic/whistler waves, with right-hand polarized magnetic fields in the solar wind plasma frame of reference and phase speed $\ll$ solar wind connection speed, are found in the regions upstream and downstream from the parallel and quasi-parallel shocks. They propagate toward upstream with wave vectors **k** nearly parallel to the magnetic field **B**. The presence of right-hand polarized beam mode and electromagnetic waves near quasi-parallel shocks has also been reported and studied by many previous simulations [e.g., *Onsager et al.*, 1991; *Scholer*, 1993]. The waves obtained in our simulation have long wavelengths $\lambda \sim 20–40c/\omega_{pi0}$ over a large distance in the foreshock. Meanwhile, wave structures with in-phase fluctuations in B and N are also present with oblique **k**'s in the 2-D plane, resulting in the crater-like structures. The parallel temperature increases in the cavities indicated in

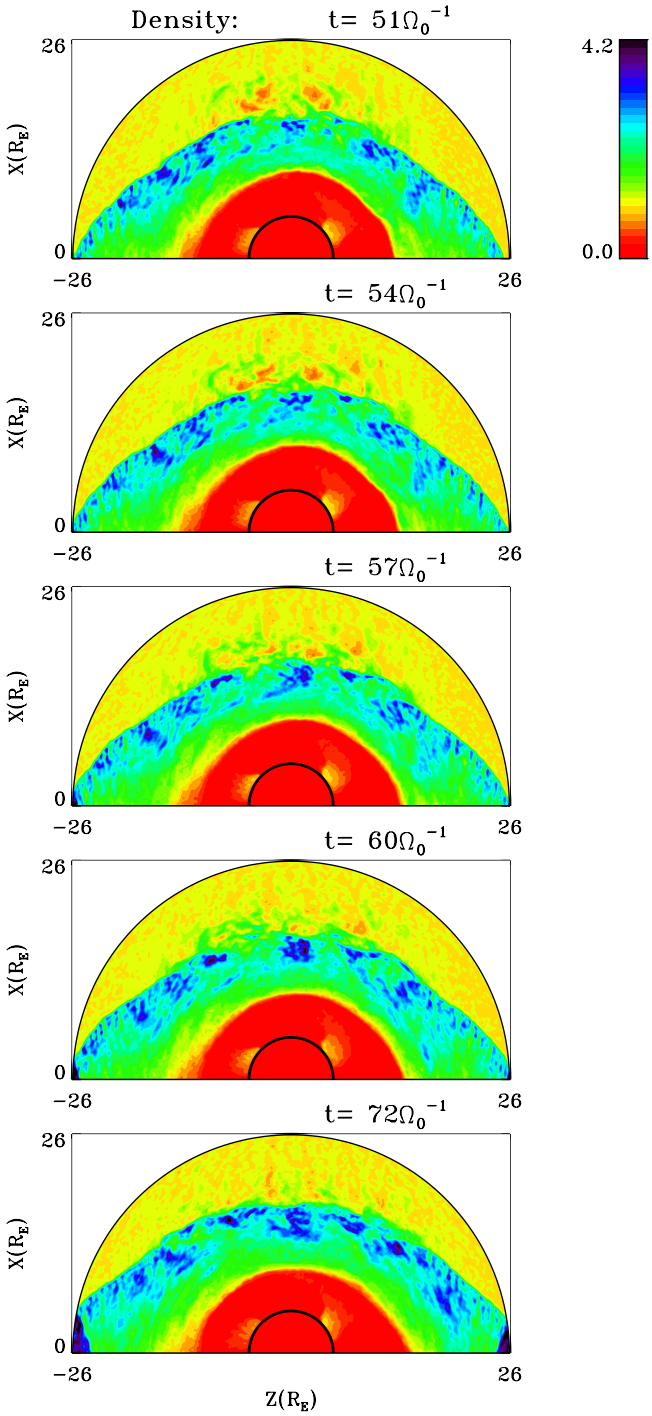

Figure 2. Ion density contours from t = 51 to $72\Omega_0^{-1}$ in case 1. The crater-like structures in the foreshock convect to the shock transition and evolve into alternate cavities and filaments elongated along field lines.

Figure 1. These craters grew from narrow compressional structures seen in contours of B and N and saturate at sizes of 1–2 R_E. The waves and the associated cavity-like structures are carried downstream by the earthward flow convection. The parallel wavelengths decrease near the shock ramp and downstream as the convection slows down.

[22] In the 2-D simulation by *Thomas and Brecht* [1988], it was shown that when a finite-sized, super-Alfvénic plasma beam moves through a background plasma, the waves excited by an electromagnetic ion beam instability can produce an energized plasma, which pushes out the

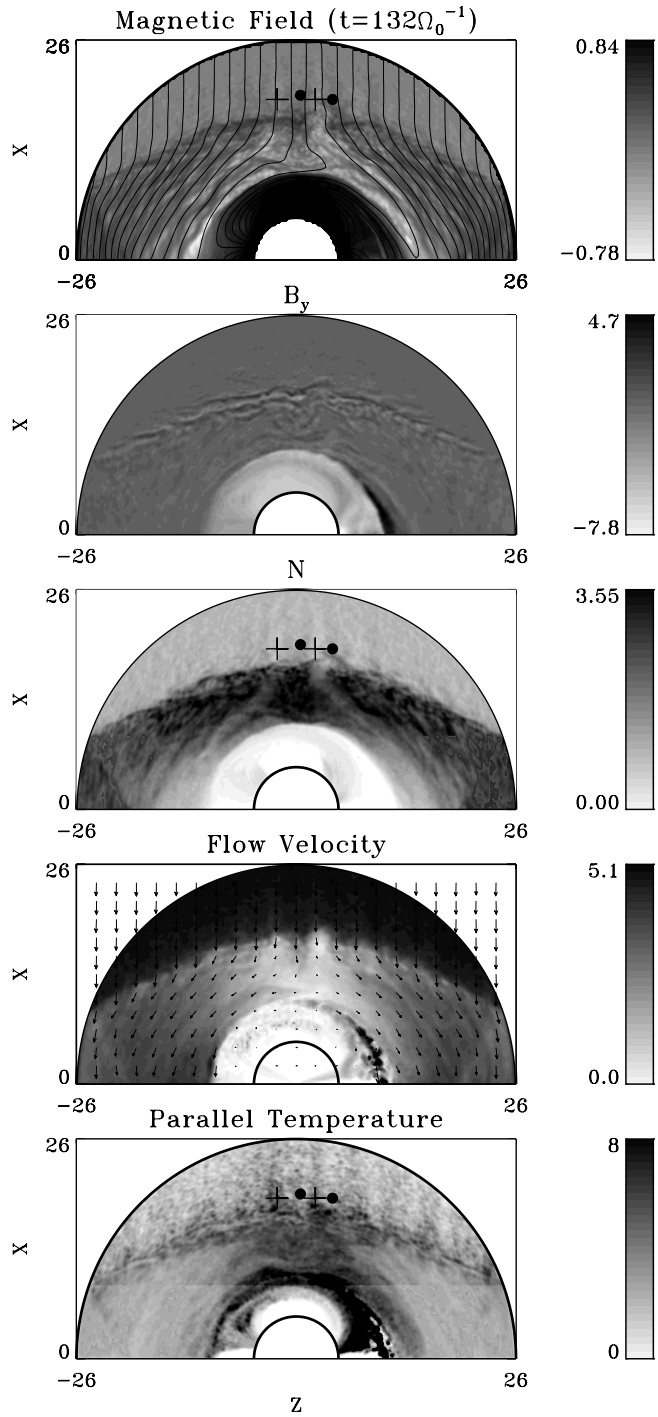

Figure 3. Simulation results at t = $132\Omega_0^{-1}$ of case 1; cavities/filaments are seen from the foreshock to the downstream magnetosheath. The upstream part of some of the cavity areas is indicated by the crosses, while the the upstream parts of some of the filaments is marked by heavy dots.

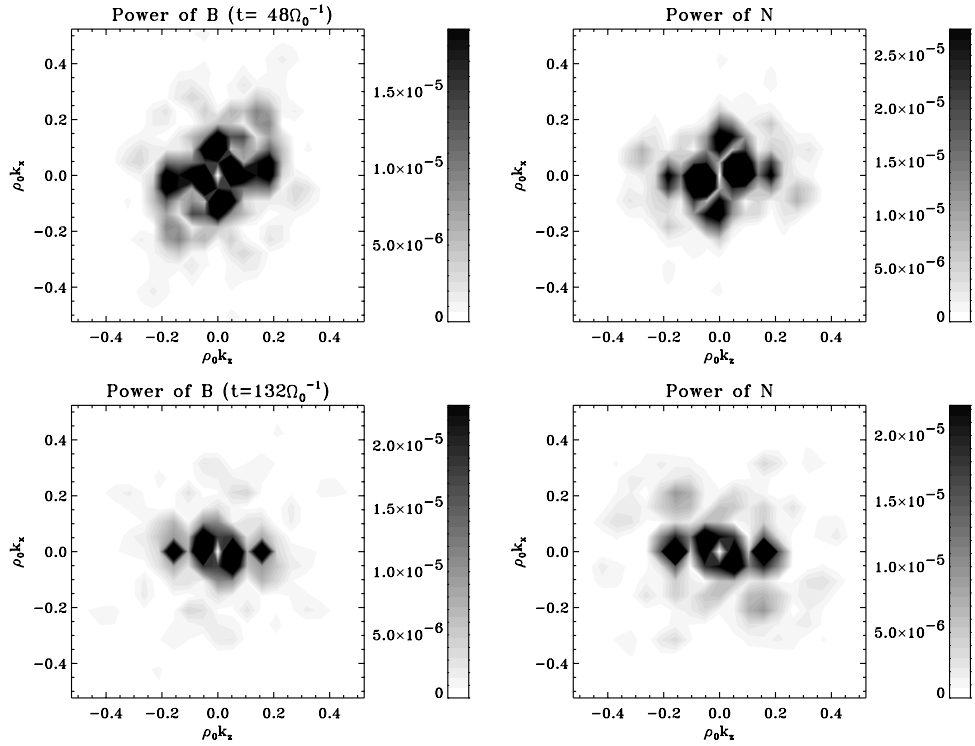

Figure 4. Power spectra of B and n in the foreshock of the quasi-parallel shock obtained from case 1, in the $k_x - k_z$ Fourier space at $t = 48$ (top row) and $132\Omega_0^{-1}$ (bottom). The wave vector k_x is nearly parallel to the IMF $\mathbf{B_0}$, and ρ_0 is the ion inertial length in the solar wind.

magnetic field and creates a diamagnetic cavity. The magnetic field and density structure of each resulting cavity in the foreshock region shown in our self-consistent simulation of the bow shock is very similar to that created by Thomas and Brecht but with many craters generated in a broad region of the foreshock. While it was suggested by Thomas and Brecht that outgoing Alfvén waves are launched from the cavity (in their case with a relative beam speed slightly larger than that in case 1 shown here), there are no Alfvén waves found in our simulation.

[23] Figure 2 shows the ion density contours in a time sequence from $t = 51$ to $72\Omega_0^{-1}$. At $t = 51$ and $54\Omega_0^{-1}$, the crater-like structures are seen to convect to the shock. By $t = 57\Omega_0^{-1}$, they have reached the shock transition, some extending into the downstream region. Meanwhile, the foreshock fluctuations are evolving with time. By $t = 72\ \Omega_0^{-1}$, they have evolved into some structures elongated along field lines in the foreshock region of the quasi-parallel shock, with alternate field-aligned filaments (with enhanced density) and cavity-like areas (with decreased density). No craters are seen anymore. The field-aligned filaments/cavities develop from the foreshock through the shock transition, with a width of $\sim 1-2\ R_E$. Note that for case 1 the craters seem to be present only in early times of the evolution of quasi-parallel shocks, corresponding to a short IMF connection time.

[24] Figure 3 shows the results of case 1 at $t = 132\Omega_0^{-1}$. These alternate filaments/cavities have extended through the shock transition, following streamlines into the downstream magnetosheath. These filaments/cavities in downstream are also aligned with the streamlines, resulting in layered magnetosheath. The upstream parts of some of the cavity areas are indicated by the crosses, while the upstream parts of some of the filaments are marked by heavy dots. In the increased-density filaments (decreased-density cavities), the magnetic field also increases (decreases), although the dips in density and magnetic field in the decreased-density areas of the foreshock are not as significant as those at earlier times. Similar to the foreshock craters at earlier times, the corresponding structures in the parallel temperature are in an antiphase correlation with N or B, with an enhanced $T_{\|}$ in the cavity areas. These field-aligned structures are phase-standing in the plasma frame, and thus stationary in the simulation (Earth) frame in this case with flow velocities $\mathbf{V}$ nearly parallel to $\mathbf{B}$. On the other hand, waves with right-hand polarizations in B_y and B_z (not shown) remain in the downstream region but with much shorter wave lengths compared to those in Figure 1. Near the shock transition, a mixture of right-hand and left-hand polarized waves are found.

[25] Perhaps the most noticeable effects, shown in Figure 3, of the foreshock cavities on the magnetosheath is the transmission of the compressional structures from the upstream region into the downstream. While in case 1 with $\mathbf{B}$ nearly $\|$ $\mathbf{V}$ everywhere upstream and downstream (and with constant IMF and solar wind conditions), the cavities develop into the phase-standing spatial structures and extend earthward from the foreshock, in general cases with the magnetic field $\mathbf{B}$ oblique to $\mathbf{V}$, the field-aligned cavities/filaments can convect as transient structures oblique to the flow. A case with the IMF oblique to the solar wind flow will be shown later. Note that if the IMF and solar wind conditions are variable so that the lifetime of a quasi-parallel shock is short, the foreshock

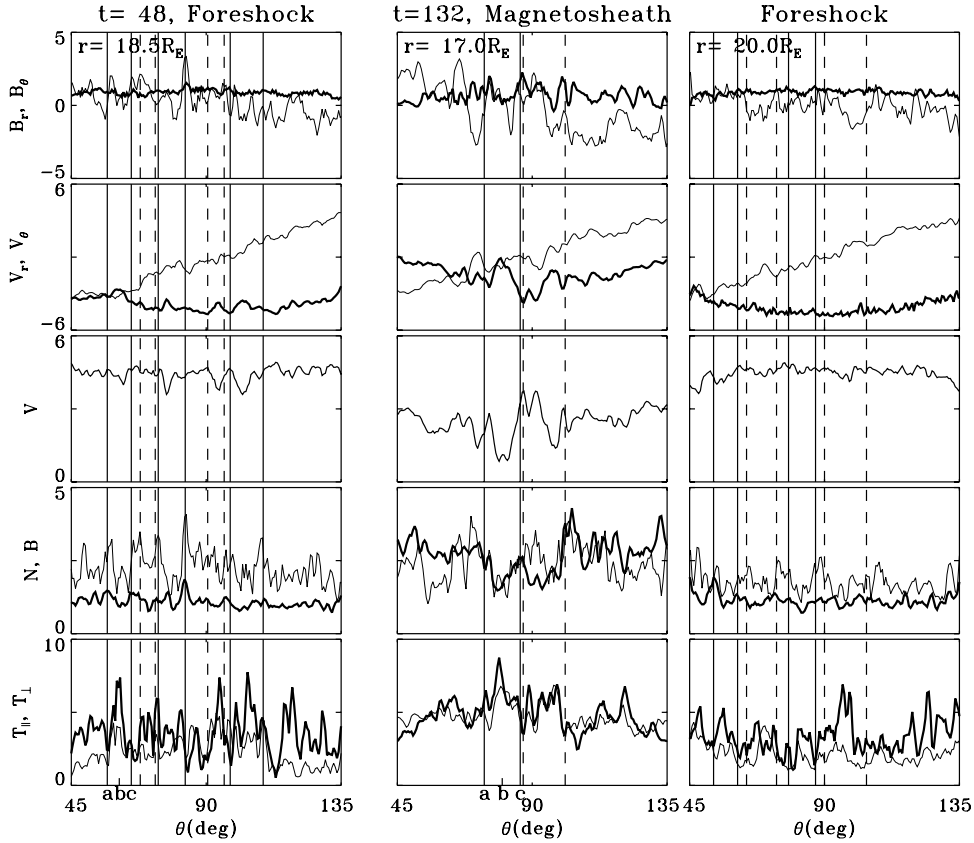

Figure 5. Left column: Spatial profiles of the magnetic field components B_r (heavy solid line) and B_θ (light solid line), ion flow components V_r (heavy) and V_θ (light), flow speed V, ion density N (heavy), field magnitude B (light), and the ion temperature components $T_{\|}$ (heavy) and $T_\perp$ (light) along the coordinate line with r = 18.5 R_E in the foreshock, from θ = 45° in the Northern Hemisphere to θ = 135° in the Southern Hemisphere, at time $t = 48\Omega_0^{-1}$. Right two columns: Results along r = 20.0 R_E in the foreshock and r = 17.0 R_E in the downstream region at $t = 132\Omega_0^{-1}$. Some regions with decreased B and N are marked by a pair of solid, or dashed, vertical lines bounding each region from north and south.

cavities can convect to the magnetopause as transient compressional structures.

[26] In order to see the evolution of the foreshock structures from craters in earlier times to the later field-aligned patterns in case 1, here we examine the evolution of the power spectra of N and B. Figure 4 shows the power spectra of B and n associated with the compressional variations, in the foreshock of the quasi-parallel shock, in the $k_x - k_z$ Fourier space at t = 48 and $132\Omega_0^{-1}$, where k_x and k_z are the wave vectors in the x (parallel to the IMF) and z directions. The results at $t = 48\Omega_0^{-1}$ are obtained from the magnetic field and density in the region from $z = -4.0$ R_E to +4.0 R_E and x = 17.5 R_E to 25.5 R_E, while the results at $t = 132\Omega_0^{-1}$ are obtained from data in the region from $z = -3.5$ R_E to +3.5 R_E and x = 18.0 R_E to 25.0 R_E. It is seen that the fluctuations in B and N are indeed well correlated. At $t = 48\Omega_0^{-1}$, fluctuations in B and N are at wave vectors **k** in nearly all the directions, corresponding to the crater-like structures. Large power values are seen at (1) $|k_x|\rho_0 \sim 0.1$, $|k_z| \sim 0$, (2) $|k_x|\rho_0 \sim 0.06$, $|k_z|\rho_0 \sim 0$, and (3) $|k_x|\rho_0 \sim 0.17$, $|k_z|\rho_0 \sim 0.03$, where ρ_0 is the ion inertial length in the solar wind. The first mode has **k** nearly $\| \mathbf{B_0}$, while the latter two modes indicate some nearly perpendicularly propagating compressional structures. Later at $t = 132\Omega_0^{-1}$, only modes with **k** nearly $\perp \mathbf{B_0}$ are dominant, and the mode with $k \sim k_{\|}$ has almost disappeared in the power spectra of B and N for the foreshock region, as seen in the bottom plots of Figure 4. This final mode corresponds to the field-aligned alternate filaments/cavities. Note that wave perturbations in B_y and B_z are also seen in the foreshock (and downstream) regions, but they are not correlated with these structures in B and N.

[27] To present the details of the foreshock structures and their downstream extension in case 1 shown here, Figure 5 depicts the spatial profiles of the magnetic field components B_r and B_θ, ion flow components V_r and V_θ, flow speed V, field magnitude B, ion density N, and the ion temperature components $T_{\|}$ and $T_\perp$ along some coordinate lines with a constant radius r, from location θ = 45° in the Northern Hemisphere to θ = 135° in the Southern Hemisphere. Shown in the left column of Figure 5 are various quantities along r = 18.5 R_E in the foreshock at earlier time $t = 48\Omega_0^{-1}$, whereas the two columns on the right show the results along r = 20.0 R_E in the foreshock and r = 17.0 R_E in the downstream region at $t = 132\Omega_0^{-1}$, when the cavities and filaments have developed from the foreshock to downstream. Some regions with decreased B and N are marked by a pair of solid, or dashed, vertical lines bounding each region from north and south. As described earlier, at $t = 48\Omega_0^{-1}$, the low density, low magnetic field, and low

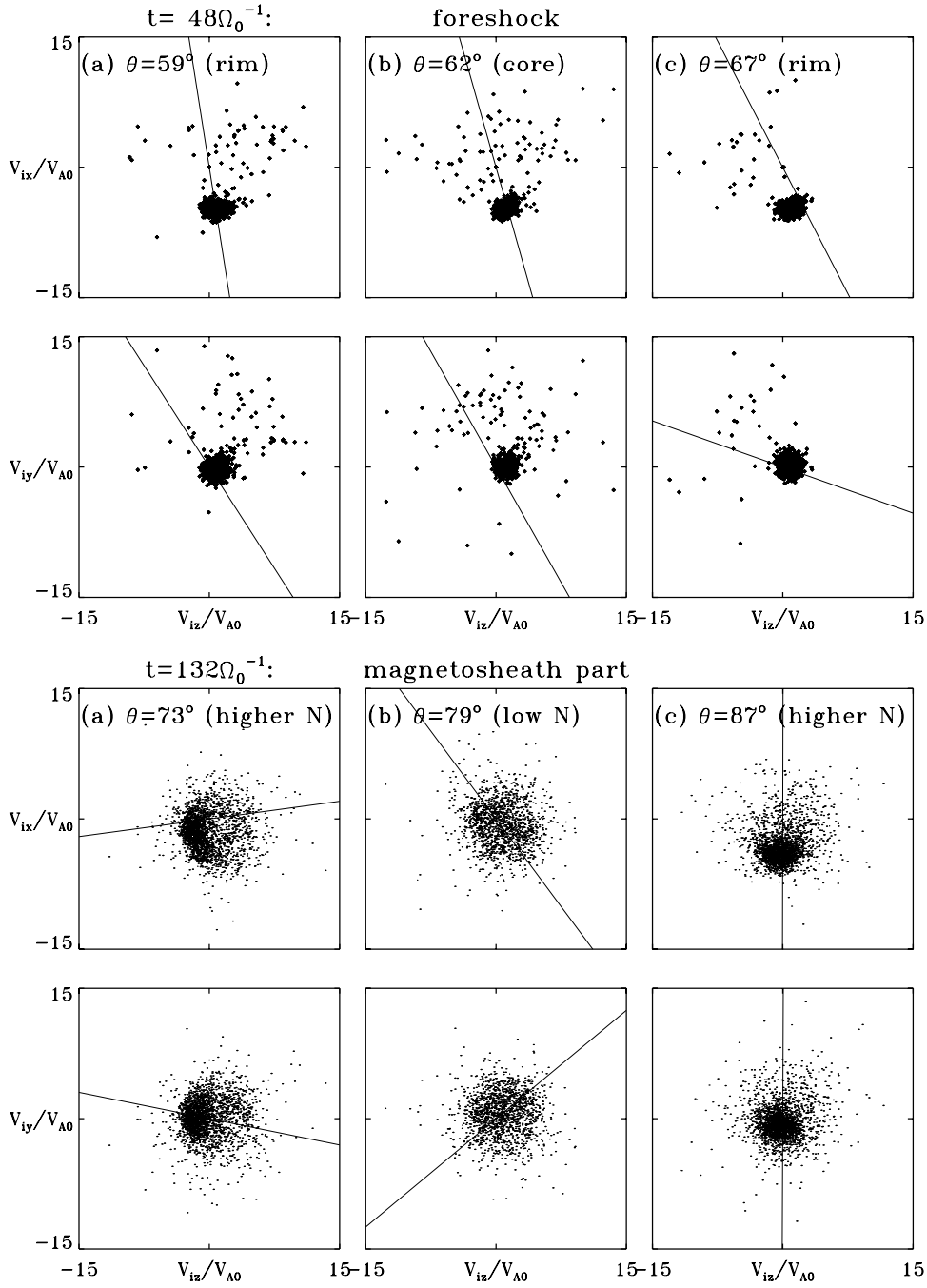

Figure 6. Ion velocity distributions: scatter plots in the velocity ($\mathbf{v_i}$) space for ions at locations "a," "b," and "c" indicated on the θ-axis in Figure 5, around the foreshock (top two rows) and downstream (bottom two rows) cavities. The straight line in each plot is along the local magnetic field direction.

flow speed regions are bounded by enhanced N and B around the foreshock cavities. At $t = 132\Omega_0^{-1}$ after the craters have developed into field-aligned structures, the amplitudes of the alternate increases and decreases in B and N in the foreshock have been reduced. The two low density regions indicated for the magnetosheath at $t = 132\Omega_0^{-1}$ are the corresponding downstream parts of the field-aligned foreshock structures around $\theta \simeq 82°$ and 97°. Similar to their foreshock counterpart, B, N, and V have an in-phase correlation in these downstream structures. For example, for the foreshock cavity centered at $\theta = 82°$ (or at the 8° latitude) at $t = 132\Omega_0^{-1}$, the magnetic field decreases by ∼45% compared with the enhanced values in the ambient filaments surrounding the cavity, and the density decreases by ∼30%. The temperature increases by a factor of 2, but the flow speed decreases by only ∼5% in this cavity. In its downstream counterpart centered at $\theta = 79°$ at $r = 17\ R_E$, as seen in the middle column of Figure 5, B decreases by ∼50% compared with the increased magnetic field in the surrounding filaments, and N decreases by ∼45%. The temperature increases by a factor of 1.5. Note that the flow speed is also reduced by ∼50% in the magnetosheath cavity.

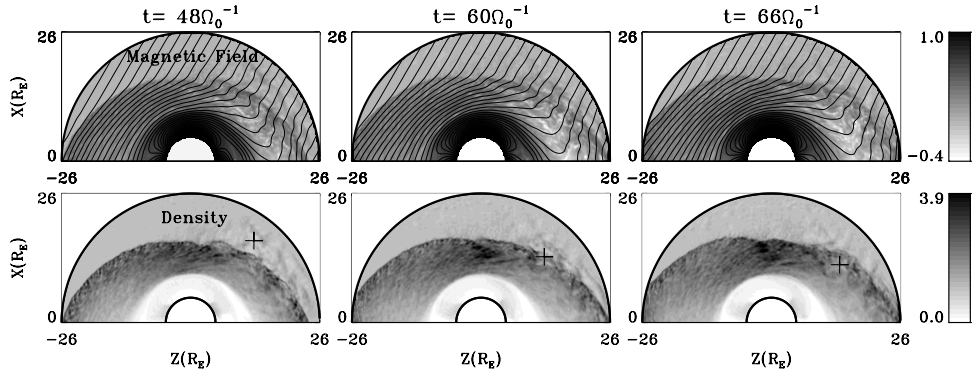

Figure 7. Magnetic field lines, on top of the field magnitude B on the logarithmic scale, and the ion number density N at $t = 48$ (left column), 60 (middle), and $66\Omega_0^{-1}$ (right) obtained from case 2 with the IMF pointing at 30° angle from the Sun-Earth line. The cavity indicated by the cross mark propagates from the foreshock into the magnetosheath.

[28] While both temperatures $T_{\|}$ and $T_{\perp}$ increase in the downstream field-aligned cavities at $t = 132\Omega_0^{-1}$, the perpendicular ion temperature $T_{\perp}$ does not always increase as much as $T_{\|}$ in the foreshock cavities, as shown in Figure 5 for both $t = 48$ and $132\Omega_0^{-1}$. The increase in $T_{\|}$ in most of these foreshock cavities indicates the presence of energetic ion particles. To see the corresponding ion phase space behavior, we show in Figure 6 the ion scatter plots in the velocity ($\mathbf{v_i}$) space for ions at locations "a," "b," and "c," as indicated on the θ-axis in Figure 5, around the foreshock and downstream cavities. Here, locations "a" and "c" are at the rims or boundary filaments around the cavities, where the density increases, and location "b" is in the center of the low density areas. The top two rows of Figure 6 show the ion velocity distributions through a crater in the foreshock, at $t = 48\Omega_0^{-1}$. All the velocities shown are normalized to the Alfvén speed V_{A0} in the solar wind. The straight line in each plot is along the local magnetic field direction in the corresponding plane. At the rim locations with θ = 59° and 67°, the hot, tenuous, backstreaming beam ions and the cold, dense, incident solar wind ion population are present. It is seen that the speeds of the hot ions can reach beyond $15V_{A0}$, while the bulk flow speed of the much colder incident solar wind ions is $\sim 5V_{A0}$. At location "b" in the center of the crater the two populations and their peak speeds can still be clearly distinguished. The hot population, though, is found to become somewhat more isotropic in the direction perpendicular to $\mathbf{B_0}$. The distribution in the foreshock cavity is very different from that in hot flow anomalies obtained in our previous simulations [*Lin*, 2002], in which the interaction between the specularly reflected, multiple ion beams caused an isotropic ion distribution in the HFA.

[29] The bottom two rows of Figure 6 show the ion distributions around a cavity area in the downstream at $t = 132\Omega_0^{-1}$. The cavity is evolved from upstream, and at this distance ($r = 17\ R_E$) not far from the shock transition, the distribution in the high-density filaments around the diamagnetic cavity still consists of two populations: the somewhat slowed and heated incident solar wind ions coexist with the heated ions in downstream, as shown in the left and right columns for locations "a" (at θ = 73°) and "c" (θ = 87°). In the low-density center at location "b" for θ = 79°, however, only an isotropic, hot ion distribution is present. This distribution at the low-density center is quite different from that at the center of the foreshock cavity. The ion kinetic orbits during the evolution of wave instabilities from upstream to downstream deserve further detailed study. The interaction between ions and the electromagnetic waves or diamagnetic cavities is more complicated as the cavities move through the shock transition, where a large gradient exists in the magnetic field. Multiple ion beams, including the dense beam of specularly reflected ions, are also present near the shock transition.

[30] In the above case with the IMF parallel to the solar wind flow, the field lines remain their connection to the same local shock (e.g., with certain shock normal angle) during the evolution of the shock. If the IMF is oblique to the solar wind flow, the foreshock cavities move through the foreshock regions of different local shocks as they convect to the curved shock front. The cavities thus also encounter regions with different intensities of backstreaming/reflected ion beams during their evolution. As a result, both crater-like structures, corresponding to transient evolutions of cavities, and field-aligned structures are found in the magnetosheath. In addition, since the convection velocity of field lines in the direction perpendicular to the IMF is nonzero, the connection time of field lines at quasi-parallel or quasi-perpendicular shocks is limited as they sweep along the curved shock front. The perpendicular convection speed of the upstream field lines is $\sim V_0 \sin\theta_c$, where θ_c is the angle of the IMF relative to the Sun-Earth line. Once field-aligned structures form in the foreshock, they are also found to convect in the perpendicular direction. In order to see the effects of the oblique convection on the foreshock structures at the quasi-parallel shock, we now show case 2 with the IMF pointing at a 30° angle from the Sun-Earth line. In this case, IMF $B_{x0} = 0.866B_0$, $B_{z0} = 0.5B_0$, and $B_{y0} = 0$. Other parameters are the same as in case 1.

[31] Figure 7 shows the magnetic field lines, plotted on top of the field magnitude B on the logarithmic scale, and the ion number density N at $t = 48$ (left column), 60 (middle), and $66\Omega_0^{-1}$ (right) obtained from case 2. At $t = 48\Omega_0^{-1}$, wavy magnetic field and crater-like structures are seen in the foreshock regions of the parallel and quasi-parallel shocks, which are located in the Northern Hemisphere ($z > 0$). A strong cavity, at this moment located at $x \simeq 16.5\ R_E$ and $z \simeq 12.75\ R_E$ near the parallel shock, is

indicated by the cross mark in the density plot. At $t = 60\Omega_0^{-1}$, the cavities have propagated in the $-\mathbf{x}$ direction to $x \simeq 13.25\ R_E$ closer to the shock. As seen in the middle column of Figure 7, the cavity marked by the cross sign has reached the shock transition, causing a low-density area at the shock front. Meanwhile, some field-aligned structures have developed in the foreshock of the quasi-parallel shock. By $t = 66\Omega_0^{-1}$, the marked cavity has propagated to $x \simeq 11.7\ R_E$ into the magnetosheath and is continuously moving to the magnetopause. More alternate field-aligned cavities and filaments have developed and are seen to extend into the downstream. Meanwhile, the field-aligned structures in the foreshock have convected a small distance $\sim 1.2\ R_E$ relative to those at $t = 60\Omega_0^{-1}$, northward and tailward in the direction perpendicular to the field lines. Note that later at $t = 72\Omega_0^{-1}$, some newborn craters are also present in the foreshock region of the quasi-parallel shock around $z \sim 5\ R_E$.

[32] It is expected that some of the transient compressional structures, including the craters and field-aligned structures oblique to the streamlines, may impinge on the magnetopause and cause magnetospheric waves. In the cases with IMF cone angle <45°, it is found that craters and elongated cavities/filaments can coexist and propagate in the magnetosheath downstream of the quasi-parallel shock. If the convection time of the foreshock field lines across the surface of the quasi-parallel shock is shorter than the growth time ($\sim 40\Omega_0^{-1}$) of the field-aligned structures, only craters may be present in the foreshock and propagate in the magnetosheath. However, such results are not seen in the dayside cases simulated in this paper. Overall, in general cases with the IMF oblique to the solar wind flow, localized compressional wave structures and the associated energetic particles can be launched to the magnetopause in a transient fashion. It is expected that dynamic pressure pulses may be transmitted into the magnetosphere by these compressional waves. The arrival of the compressional structures at the magnetopause is not examined in this simulation due to the limitation of the 2-D approximation. In front of the 3-D magnetopause the B_z component of the magnetic field can be carried away, antisunward around the Earth, by the V_y component of the flow. In the 2-D model, however, such V_y flow cannot form to carry away the field lines that piles up in front of the magnetopause in the general cases with $B_z \neq 0$. The excessive pileup of the field lines in front of the 2-D magnetopause artificially slows down the convection toward the magnetopause, and thus the interaction between the incoming waves and the magnetopause. The pileup of the field lines also makes it difficult to simulate the long term evolution of the bow shock, as the shock front slowly expands to the upstream boundary eventually. In addition, to catch the arrival of the transient waves at the magnetopause, high-latitude and tailside magnetopause may also need to be included in the simulation domain.

[33] The magnetic field and plasma signatures in the foreshock cavities obtained in our simulation are similar to those observed by IMP-8 and WIND in the foreshock regions [*Sibeck et al.*, 2001, 2002], with a decreased B and N bounded by enhanced magnetic field and density, and with energetic ions in the cavity. The observations also indicated that the diamagnetic cavities are very common near the quasi-parallel bow shock. The diamagnetic cavities are found at quasi-parallel shocks in all cases carried out in our simulation, with IMF cone angle of 0°–45° and Alfvén Mach number $M_A = 5 - 8$. In a high Mach number case with $M_A = 8$, the electromagnetic waves generated in the upstream in early times are found to be left-handed, but other features such as the later formation of foreshock cavities are similar to the cases shown in this paper.

[34] Finally, it should be noted that the presence of the cavity structures near the quasi-parallel shocks, as obtained in this 2-D global-scale simulation, was not reported in previous hybrid 2-D simulations of planar fast shocks. We have carried out a separate 2-D simulation of a planar fast shock with $M_A = 5$, $\theta_{Bn} = 5°$, and $\beta_0 = 0.5$, using a hybrid code similar to that used in this paper. The results are similar to those in previous 2-D simulations of the planar shock in the same parameter regime of quasi-parallel shocks [e.g., *Dubouloz and Scholer*, 1995]. No crater-like structures can be identified, although some weak field-aligned structures are found in later times ($t > 150\Omega_0^{-1}$) in B and N, more coherent near the shock transition. An interesting raised question here is what are the effects of the curved geometry of the magnetosheath on the structure of the bow shock? A difference between the planar and the curved bow shock may be that in the latter case the field lines are compressed in the dayside magnetosheath while they drape around the magnetopause. This compression may exert a magnetic mirror force on the magnetosheath ions and thus enhance the backstreaming of the downstream thermal ions to the foreshock region. As a result, the beam-plasma interaction may be stronger in the foreshock of the curved bow shock. Note that although our 2-D code may in general have exaggerated the thickness of the field compression region due to the excessive pile up of the field lines in front the 2-D magnetopause, such excessive pile up does not exist in case 1, in which **B** is nearly parallel to **V**. Further investigations are required for the theoretical understanding of the 2-D beam-plasma interaction in the vicinity of the curved bow shock, the wave-particle interaction in the formation of diamagnetic cavities, and the transmission of the foreshock cavities through the bow shock.

4. Summary

[35] It is reported in this 2-D hybrid simulation that diamagnetic cavities and filaments can develop self-consistently in the parallel and quasi-parallel bow shock. The main results on the formation and evolution of the foreshock structures and their magnetosheath component are summarized below.

[36] 1. As the bow shock forms due to the interaction between the solar wind and the geomagnetic field under fixed IMF and solar wind conditions, crater-like diamagnetic cavities are found to develop in the foreshock of the parallel and quasi-parallel shocks, where the backstreaming ions interact with the incoming solar wind ions. The center of the craters, with a low density and low magnetic field strength, is bounded by a rim with enhanced density and magnetic field. The bulk flow speed decreases in the center of the cavity, while the total ion temperature often increases. The size of the cavities saturates at $\sim 1-2\ R_E$ after an initial growth period of $\sim 20\Omega_0^{-1}$, following the formation of the bow shock.

[37] 2. These foreshock cavities propagate to the shock with the solar wind inflow, into the downstream magnetosheath. Meanwhile, they develop into field-aligned density and magnetic field structures, phase-standing in the plasma flow. In the case with IMF nearly parallel to the solar wind flow, at $t \sim 50\Omega_0^{-1}$ after the formation of the bow shock, the crater-like structures in earlier times have developed into the field-aligned structures from upstream to downstream, with alternate decrease and increase in plasma density. The corresponding variations in magnetic field are in phase with those of the density, and the flow speed also decreases slightly where the density decreases. The ion temperature often increases (decreases) with the decrease (increase) of N and B.

[38] 3. In the general cases with the IMF oblique to the solar wind, craters and field-aligned cavities/filaments convect with the flow toward the Earth as transient structures, some may impinge on the magnetopause. It is expected these compressional waves may produce dynamic pressure pulses to the magnetosphere.

[39] 4. Those field-aligned structures with a decrease in B and N and an increase in temperature appear like weak hot flow anomalies, but unlike HFAs, the formation of these structures are not due to the arrival of interplanetary discontinuities at the bow shock. The formation and evolution of the density structures in the foreshock and the downstream magnetosheath, as described above, appear to be due to the interaction between the solar wind plasma and the backstreaming/reflected ion beams in the bow shock. In early times, whistler waves are present around the shock, with wave vectors $\mathbf{k}$ parallel and oblique to the ambient magnetic field. In the final 2-D structures, the fluctuations in B and N appear to be field-aligned, with $\mathbf{k} \simeq \mathbf{k}_\perp$ in the foreshock.

[40] 5. The ion velocity distributions around the diamagnetic cavities in upstream and downstream are quite different. In the foreshock, the hot, thin ion beam and the cold, dense incoming solar wind can be clearly distinguished in both the rim and the center of the cavities. Such distribution is, again, different from that in HFAs. In the magnetosheath regions not far from the shock front, while the distributions in the high density filaments surrounding the low-density regions show the presence of the incident solar wind ion population and the hot magnetosheath plasma, only a hot, isotropic plasma population is present in the low-density cavities.

[41] While previous hybrid simulations of the interaction between an ion beam and a background plasma showed the generation of crater-like, in-phase magnetic field and ion density structures [*Thomas and Brecht*, 1988; *Thomas*, 1989], our self-consistent 2-D simulation of the bow shock shows the presence of similar diamagnetic cavities in the foreshock regions where ion beams interact with the background plasma. The simulation results seem to be quite consistent with satellite observations of the foreshock of quasi-parallel shocks. Moreover, it is found that in later times these cavities and their rims evolve into field-aligned cavities and filaments throughout the shock transition. The formation of density filaments in nonliner electromagnetic ion beam instabilities has also been found in 2-D hybrid simulations of beam-plasma interaction [*Hellinger and Mangeney*, 1999; *Wang and Lin*, 2003]. In the simulation by *Wang and Lin* [2003], the interaction between a field-aligned ion beam and a plasma leads to alternate field-aligned density and magnetic field structures in the final nonlinear stage, in addition to the Alfvén or whistler waves (evolved from the right-hand polarized, ion beam resonant instability). However, such structures do not form if the beam density is smaller than a threshold. The evolution of ion beam-plasma instabilities and the associated parametric decay through secondary instabilities will be further studied for multidimensional systems.

[42] **Acknowledgments.** This work was supported by NASA grant NAG5-12899 and NSF grant ATM-0213931 to Auburn University. Computer resources were provided by the National Partnership for Advanced Computational Infrastructure and the Arctic Region Supercomputer Center.
[43] Lou-Chuang Lee thanks Manfred Scholer and David Sibeck for their assistance in evaluating this paper.

References

Asbridge, J. R., S. J. Bame, and I. B. Strong, Outward flow of protons from the Earth's bow shock, *J. Geophys. Res.*, *73*, 5777, 1968.

Burgess, D., Cyclic behavior at quasi-parallel collisionless shocks, *Geophys. Res. Lett.*, *16*, 345, 1989.

Cahill, L. J., and V. L. Patel, The boundary of the geomagnetic field, August to November 1961, *Planet. Space Sci.*, *15*, 997, 1967.

Dubouloz, N., and M. Scholer, Two-dimensional simulations of magnetic pulsations upstream of the Earth's bow shock, *J. Geophys. Res.*, *100*, 9461, 1995.

Engebretson, M. J., N. G. Lin, W. Baumjohann, H. Luehr, B. J. Anderson, L. J. Zanetii, T. A. Potemra, R. L. McPherron, and M. G. Kivelson, A comparison of ULF fluctuations in the solar wind, magnetosheath, and dayside magnetosphere: 1. Magnetosheath morphology, *J. Geophys. Res.*, *96*, 3441, 1991.

Fairfield, D. H., W. Baumjohann, G. Paschmann, H. Luhr, and D. G. Sibeck, Upstream pressure variations associated with the bow shock and their effects on the magnetosphere, *J. Geophys. Res.*, *95*, 3773, 1990.

Fuselier, S. A., M. F. Thomsen, F. M. Ipavich, and W. K. H. Schmidt, Superthermal He^{2+} in the Earth's foreshock region, *J. Geophys. Res.*, *100*, 17,107, 1995.

Goodrich, C. C., Numerical simulations of quasi-perpendicular collisionless shocks, in *Collisionless Shocks in the Heliosphere*: *Reviews of Current Research*, *Geophys. Monogr. Ser.*, vol. 35, edited by B. T. Tsurutani and R. G. Stone, p. 153, AGU, Washington, D. C., 1985.

Gosling, J. T., and A. E. Robson, Ion reflection, gyration, and dissipation at supercritical shocks, in *Collisionless Shocks in the Heliosphere*: *Reviews of Current Research*, *Geophys. Monogr. Ser.*, vol. 35, edited by B. T. Tsurutani and R. G. Stone, p. 141, AGU, Washington, D. C., 1985.

Hellinger, P., and A. Mangeney, Electromagnetic ion beam instabilities: Oblique pulsations, *J. Geophys. Res.*, *104*, 4669, 1999.

Hoppe, M. M., C. T. Russell, L. A. Frank, T. E. Eastman, and E. W. Greenstadt, Upstream hydromagnetic waves and their association with backstreaming ion populations: ISEE 1 and 2 observations, *J. Geophys. Res.*, *86*, 4471, 1981.

Krauss-Varban, D., Waves associated with quasi-parallel shocks: Generation, mode conversion, and implications, *Adv. Space Res.*, *15*, 271, 1995.

Lee, M. A., Coupled hydromagnetic wave excitation and ion acceleration upstream of the Earth's bow shock, *J. Geophys. Res.*, *87*, 5063, 1982.

Leroy, M. M., and D. Winske, Backstreaming ions from oblique Earth bow shocks, *Ann. Geophys.*, *1*, 527, 1983.

Lin, Y., Generation of anomalous flows near the bow shock by its interaction with interplanetary discontinuities, *J. Geophys. Res.*, *102*, 24,265, 1997.

Lin, Y., Global hybrid simulation of hot flow anomalies near the bow shock and in the magnetosheath, *Planet. Space Sci.*, *50*, 577, 2002.

Lin, Y., D. W. Swift, and L. C. Lee, Simulation of pressure pulses in the bow shock and magnetosheath driven by variations in interplanetary magnetic field direction, *J. Geophys. Res.*, *101*, 27,251, 1996.

Lyu, L. H., and J. R. Kan, Ion leakage, ion reflection, ion heating, and shock-front reformation in a simulated supercritical quasi-parallel collisionless shock, *Geophys. Res. Lett.*, *17*, 1041, 1990.

Onsager, T. G., D. Winske, and M. F. Thomsen, Interaction of a finite-length ion beam with a background plasma: Reflected ions at the quasi-parallel bow shock, *J. Geophys. Res.*, *96*, 1775, 1991.

Russell, C. T., J. G. Luhmann, T. J. Odera, and W. F. Stuart, The rate of occurrence of dayside Pc 3, 4 pulsations: The L-value dependence of the IMF cone angle effect, *Geophys. Res. Lett.*, *10*, 663, 1983.

Scholer, M., Upstream waves, schocklets, short large-amplitude magnetic structures and the cyclic behavior of oblique quasi-parallel collisionless shocks, *J. Geophys. Res.*, *98*, 47, 1993.

Scholer, M., and T. Terasawa, Ion reflection and dissipation at quasi-parallel collisionless shocks, *Geophys. Res. Lett.*, *17*, 119, 1990.

Scholer, M., M. Fujimoto, and H. Kucharek, Two-dimensional simulations of supercritical quasi-parallel shocks: Upstream waves, downstream waves, and shock reformation, *J. Geophys. Res.*, *98*, 18,971, 1993.

Schwartz, S. J., R. L. Kessel, C. C. Brown, L. J. C. Woolliscroft, M. W. Dunlop, C. J. Farrugia, and D. S. Hall, Active current sheets near the Earth's bow shock, *J. Geophys. Res.*, *93*, 11,295, 1988.

Schwartz, S. J., D. Burgess, W. P. Wilkinson, R. L. Kessel, M. Dunlop, and H. Luhr, Observations of short large-amplitude magnetic structures at a quasi-parallel shock, *J. Geophys. Res.*, *97*, 4209, 1992.

Sckopke, N., G. Paschmann, S. J. Bame, J. Gosling, and C. T. Russell, Evolution of ion distributions across the nearly perpendicular bow shock: Specularly and non-specularly reflected ions, *J. Geophys. Res.*, *88*, 6121, 1983.

Sibeck, D. G., et al., The magnetospheric response to 8-minute-period strong-amplitude upstream pressure variations, *J. Geophys. Res.*, *94*, 2505, 1989.

Sibeck, D. G., R. B. Decker, D. G. Mitchell, A. J. Lazarus, R. P. Lepping, K. W. Ogilvie, and A. Szaba, Solar wind preconditioning in the flank foreshock: IMP-8 observations, *J. Geophys. Res.*, *106*, 21,675, 2001.

Sibeck, D. G., T.-D. Phan, R. Lin, R. P. Lepping, and A. Szabo, Wind observations of foreshock cavities: A case study, *J. Geophys. Res.*, *107*(A10), 1271, doi:10.1029/2001JA007539, 2002.

Sibeck, D. G., N. B. Trivedi, E. Zesta, R. B. Decker, H. J. Singer, A. Szabo, H. Tachihara, and J. Watermann, Pressure-pulse interaction with the magnetosphere and ionosphere, *J. Geophys. Res.*, *108*(A2), 1095, doi:10.1029/2002JA009675, 2003.

Swift, D. W., Use of a hybrid code for a global-scale plasma simulation, *J. Comput. Phys.*, *126*, 109, 1996.

Tanaka, M., C. C. Goodrich, D. Winske, and K. Papadopoulos, A source of backstreaming ion beams in the foreshock region, *J. Geophys. Res.*, *88*, 3046, 1983.

Thomas, V. A., Three-dimensional simulation of diamagnetic cavity formation by a finite-sized plasma beam, *J. Geophys. Res.*, *94*, 13,579, 1989.

Thomas, V. A., and S. H. Brecht, Evolution of diamagnetic cavities in the solar wind, *J. Geophys. Res.*, *93*, 11,341, 1988.

Thomas, V. A., D. Winske, and N. Omidi, Reforming supercritical quasi-parallel shocks: 1. One and two dimensional simulations, *J. Geophys. Res.*, *95*, 18,809, 1990.

Wang, X. Y., and Y. Lin, Generation of nonlinear Alfvén and magnetosonic waves by beam plasma interaction, *Phys. Plasmas*, *10*, 3528–3538, 2003.

Wibberenz, G., F. Zollich, H. M. Fischer, and K. Keppler, Dynamics of intense upstream ion events, *J. Geophys. Res.*, *90*, 283, 1985.

Winske, D., N. Omidi, K. B. Quest, and V. Thomas, V. A., Reforming supercritical quasi-parallel shocks: 2. Mechanism for wave generation and front reformation, *J. Geophys. Res.*, *95*, 18,821, 1990.

Y. Lin, Physics Department, Auburn University, 206 Allison Laboratory, Auburn, AL 36849-5311, USA. (ylin@physics.auburn.edu)